applied sciences

MDPI

Article

Study on the Influence of Rock Shape on Rolling Distance

Feng Liu [1], Ning Hu [1], Gangchen Sun [1,2,*] and Bai Yang [3,*]

[1] Academy of Civil and Architectural Engineering, Guilin University of Technology, Guilin 541004, China; 6616019@glut.edu.cn (F.L.); 2120210696@glut.edu.cn (N.H.)
[2] Guangxi Key Laboratory of Geotechnical Mechanics and Engineering, Guilin 541004, China
[3] School of Architecture and Transportation Engineering, Guilin University of Electronic Technology, Guilin 541004, China
* Correspondence: sun2963@163.com (G.S.); ayangbai@163.com (B.Y.)

Abstract: To explore the influence of rock shape on rolling distance and effectively mitigate rockfall hazards, the following research was conducted. Factors influencing the rolling distance of rocks were determined through model experiments, and the mechanics of rolling resistance were analyzed. The coefficient RF, reflecting the ease of rock rolling, and the shape parameter ψ, quantifying the rolling distance, were proposed. By incorporating the shape parameter into kinematic equations, formulas for calculating the rolling distance of rocks with varying shapes on diverse ground characteristics were derived. These formulas underwent validation using data from model experiments, revealing minimal disparities between the experimental and calculated values. Irregularities on the rolling surface, commonly referred to as "steps" due to the differences in surface hardness among various materials, as well as deviations and shifts in the rolling axis during rock movement, were identified as the primary factors influencing rolling distance and contributing to calculation errors. Combining these deviations for rocks of distinct shapes with theoretical formulas enabled the determination of the range of influence of rock rolling at various velocities, offering valuable insights for assessing areas prone to rockfall hazards.

Keywords: rock shape; rolling distance; model testing; sensitive parameters; rockfall prevention

Citation: Liu, F.; Hu, N.; Sun, G.; Yang, B. Study on the Influence of Rock Shape on Rolling Distance. *Appl. Sci.* **2023**, *13*, 11351. https://doi.org/10.3390/app132011351

Academic Editors: Peng Huang, Nan Zhou and Meng Li

Received: 11 September 2023
Revised: 8 October 2023
Accepted: 11 October 2023
Published: 16 October 2023

1. Introduction

China is a mountainous country with mountainous regions covering 1/3 of the country's total land area. These mountainous areas are particularly prone to geological hazards, with rockfall disasters being a prominent concern. In 2022 alone, China experienced 1366 cases of landslide disasters, representing 24.14% of the total geological disasters in the nation. These events pose a substantial threat to the safety of lives and property, as depicted in Figures 1 and 2. Rockfall is the process and phenomenon in which rock masses of various sizes detach from their source areas and accumulate at the base of slopes through falling, bouncing, rolling, sliding, and other movements [1]. For areas within mountainous regions, including residential areas, transportation routes, pipelines, bridges, and more, a crucial component of rockfall hazard assessment involves delineating hazardous zones beneath rock walls. Determining the distance traveled by rockfall is essential for evaluating these hazard zones [2].

In the investigation and study of diverse rockfall-prone areas, it is evident that factors impacting the rolling distance of rockfall encompass many characteristics: terrain conditions, such as slope angle, release height, slope surface roughness, and vegetation coverage [3–7]; the geomechanical properties of the slope, including particle size, void ratio, moisture, and hardness [8,9]; the three-dimensional nature of slopes, including lateral, vertical, valley, and channel dimensions [10]; and the roughness of the slope surface, including the size and shape of the surface coverings [11,12]. Moreover, the properties of the rockfall itself, including its size, shape, and lithology, are intimately linked to the rolling

distance [13–15]. Notably, the size and shape of the rockfall, along with their interaction with the slope surface during rolling, are recognized as pivotal factors influencing the rolling distance [8,16,17]. By quantifying these influential factors and incorporating them into calculation models, we can predict the rolling distance of rockfall [18–20].

Figure 1. A rockfall disaster in Hechi City, China.

Figure 2. A rockfall disaster on a rural road in Enshi City, China.

Presently, widely adopted empirical models for predicting rockfall hazard areas involve the utilization of arrival angles [21] and shadow angles [22]. These empirical models rely on the statistical analysis of data from previous rockfall events within the study area, resulting in functional formulas [23] applicable for predicting rockfall rolling distance, not only within the study area but also in regions sharing similar geological conditions. For instance, Copons et al. [24] analyzed rockfall motion distance, utilizing geometric methods, and introduced an empirical model to estimate the rolling distance based on the rockfall's initial height and horizontal component. Yang et al. [25] took into account the impact of intergranular friction on the propagation distance of rockfall and, by integrating the effects of friction weakening during rolling, formulated a calculation model for rockfall rolling

distance. Within a kinematic framework, Zhang et al. [2] introduced a mathematical model for rolling distance, considering the influence of self-rotation of rockfall.

Currently, research on the impact of rockfall characteristics, including shape, size, and slope surface hardness, on rolling distance is relatively scarce [26–29]. Primary research methods encompass model experiments [30,31], case analysis [24], and numerical simulations [32–34]. In this context, Nagendran et al. [30] discovered that rockfall's own shape notably influences rolling distance, with near-spherical and gently inclined rockfall covering greater distances. They also proposed that the trajectory of rockfall can be predicted based on its shape and size. Zhang et al. [35] introduced a method for generating intricate geometric shapes through 3D reconstruction, which was utilized to investigate the impact of rock block shape and size on motion and energy conversion. Wang et al. [36] employed orthogonal experimental methods to assess the sensitivity of factors influencing the horizontal movement distance of rockfall. They developed a predictive system for rockfall movement that incorporates factors like slope height, slope angle, and mass. Caviezel et al. [37], by analyzing field test data, quantified the influence of rockfall shape and mass on lateral spreading and longitudinal displacement. They highlighted that rockfall shape significantly affects its motion characteristics. Additionally, Torsello et al. [38] observed that spherical rockfall, in comparison to irregularly shaped rockfall, exhibits a longer rolling distance. Liu et al. [39] highlighted that energy loss during the rolling process of rolling bodies primarily results from rolling frictional resistance, and the magnitude of this resistance relies on the shape, material, and surface characteristics of the rolling body.

In summary, our understanding of how rockfall motion characteristics are influenced by their shape has been steadily expanding, highlighting the significance of shape as a critical factor in determining their rolling distance. Nonetheless, the prevailing formulas employed for estimating rockfall travel distance primarily comprise empirical models derived from regional rockfall disaster data and kinematic formulas that do not account for the impact of rockfall shape. Consequently, the ongoing research into the mechanism by which rockfall shape influences rolling distance lacks depth, and the correlation between rockfall shape and rolling distance remains unquantifiable. This limitation hampers our ability to assess the extent of rockfall's impact on the ground.

This study utilizes a model test device to simulate rockfall scenarios on the ground. By altering the shape of the test block, its rolling speed, and the ground material, we obtain variations in the rolling distance of the test block under the influence of different factors. The experiments reveal that the rolling resistance of the test block is contingent on its interaction with the ground during rolling. This interaction encompasses the two-dimensional cross-sectional shape of the test block during rolling and the extent of ground deformation. The rolling resistance attributable to the shape of the test block is denoted as the coefficient RF, quantifying how rockfall shape impacts the rolling distance. This parameter is integrated into the kinematic formula, yielding formulas for calculating rockfall rolling distance on various terrain features. The accuracy of the formulas is confirmed via a comparative analysis between model test data and results derived from the formulas. Following verification in field tests, these formulas can be used as a reference for rockfall hazard assessment and protective design.

2. Model Test

2.1. Determining the Influence of Rockfall Shape on Its Rolling Characteristics

2.1.1. Test Device

The first step of designing model tests is to determine the ratio between the actual dimensions of rock blocks/slopes in rockfall disasters and the test model, known as the similarity scale [40,41]. Previous studies have investigated and analyzed different historical rockfall disasters and found that the size of rockfall debris ranges from tens of centimeters to several meters [42], weighing hundreds of tons, and that the volume of individual debris can reach more than 1000 cubic meters [41,43]. Therefore, in order to better restore the size

of rock blocks in real rockfall disasters, the geometric ratio is set to 50, and the gravity and time similarity ratios are set to one in the model test.

The test device comprises four main components: the release chute for the test block, the rolling surface, velocity measurement devices, and a rolling trajectory recording apparatus, as illustrated in Figure 3. The surface of the release chute is made of rigid ceramic tiles. The chute's release angle and height can be adjusted using the lifting rods on the frame to attain the desired initial slope and velocity for the experiments.

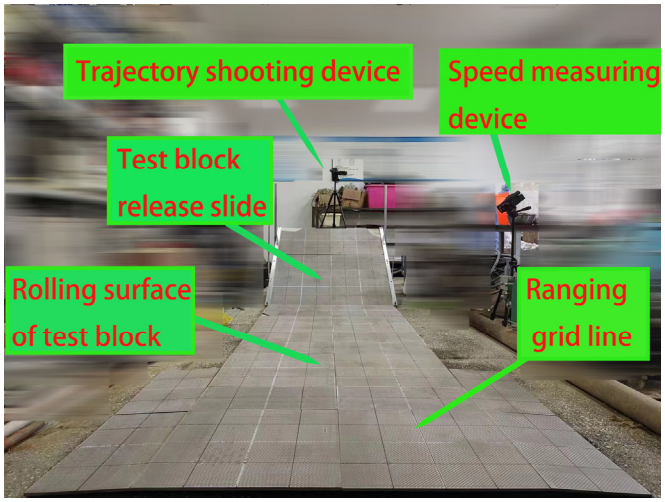

Figure 3. Test device.

Given that the slope can influence the motion characteristics of rockfalls, Wong [44] noted that when the release slope exceeds 45°, the rockfall will directly impact the rolling surface upon leaving the chute, leading to significant jumps and substantial energy consumption. Only by maintaining uninterrupted contact with the ground during the rockfall's motion can we measure the shape's influence on rolling distance; therefore, the release slope was restricted to a lower range (20–40°) to prevent jumping upon exit from the chute.

To confirm the suitability of the theoretical formulas for composite terrain surfaces, diverse rolling experiments were devised. These encompassed rolling the test block on singular materials and surfaces composed of multiple materials. The materials for the rolling surface were chosen to replicate distinct site features, such as exposed bedrock or smooth rocky slopes, soft rock, and rocky slopes with vegetation [43], as shown in Figure 3.

Gridlines were drawn on the rolling surface to aid in measuring the rolling distance of the test block. Velocity measurement and trajectory recording were accomplished using two high-speed cameras. The velocity camera was positioned on the right side at the end of the release chute to record the initial velocity of the rockfall after it left the chute. The trajectory camera was placed above the release slope to capture the complete trajectory, from the moment the rockfall exited the chute until it came to a stop.

2.1.2. Test Blocks

When selecting the shape of the test rockfall, reference was made to three typical rockfall shape characteristics among several typical rockfall shapes that are prone to inducing rockfall disasters in mountainous areas [45], including spherical, cylindrical, and disc-shaped rockfall. Considering the similarity of model tests, materials with densities and hardness similar to those of actual rolling stones were selected for the test block. The non-spherical test block used to simulate the rolling stone in the test was poured from C60 concrete, the mix ratio of C60 concrete is shown in Table 1, while the spherical test block was cut from granite, as shown in Figure 4. When determining the center of gravity of the test block, the test block was placed in a three-dimensional coordinate system, and the section with the minimum rolling resistance coefficient RF was tangent to the coordinate plane formed by the x-axis and z-axis. The two-dimensional section perpendicular to the

test block and the section was tangent to the coordinate plane formed by the *y*-axis and *z*-axis. This could determine the center of gravity of the test block. The specific shape parameters are shown in Table 2.

Table 1. Ingredients of C60 concrete grouting materials.

Materials	Po52.5 Cement	8–20 Mesh Quartz Stone	20–80 Mesh Quartz Stone	Fly Ash	Silica Fume	Water
Material Usage (%)	37	10	45	5	3	12.5
Additive	ZY808 Defoamer	ZY1100 Plastic Expansion Agent	ZY8121 Water Reducing Agent	MK400 Cellulose		
Dosage per 100 kg (g)	30	20	130	15		

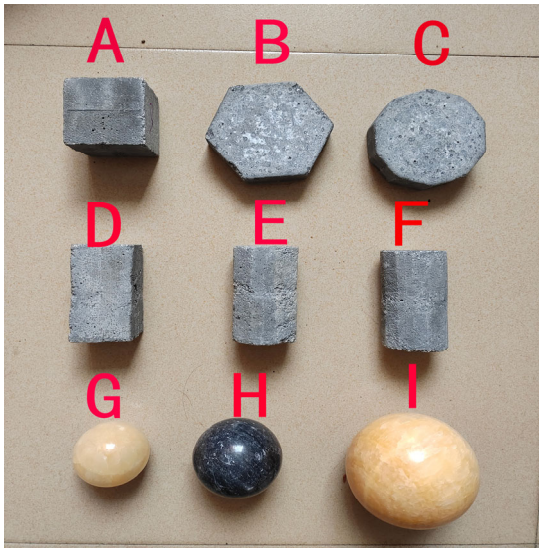

Figure 4. Test blocks.

Table 2. Shape parameters of test blocks.

Test Block	Shape	Characteristic Length	Value (mm)	Volume (cm^3)	Center of Gravity (mm) x/y/z	Shape Parameter RF	Shape Parameter ψ_1/ψ_2	Density (kg/m)	Mass (g)
A	Regular hexahedron	Edge length	56	175.6	28/28/28	1	0.36	2460	432
B	6-edged disk	Edge length/height	50/27	175.4	43.3/13.5/43.3	0.58	0.17	2463	432
C	12-edged disk	Edge length/height	23/30	174.9	43/11.5/43	0.3	0.04	2493	436
D	4-edged prism	Length/width/height	45/45/88	178.2	22.5/44/22.5	1	0.36/0.48	2452	437
E	8-edged prism	Edge length/height	20/90	173.8	24.7/45/24.7	0.4	0.1/0.45	2457	427
F	12-edged prism	Edge length/height	13/91	172.2	24.2/45.5/24.2	0.27	0.06/0.44	2456	423
G	Sphere 1	Diameter	60	113	3/3/3	0	0	2673	302
H	Sphere 2	Diameter	70	179.5	3.5/3.5/3.5	0	0	2670	483
I	Sphere 3	Diameter	100	523.3	5/5/5	0	0	2430	1062

During the test, by adjusting the slope of the release ramp, different shapes of test blocks are released from different positions on the slope, allowing them to roll or slide downward under the action of gravity, in order to obtain any initial rolling speed required for the test block. The initial velocity of the test block after leaving the slope surface was

obtained through a speed measurement device, and the rolling condition of the test block on the rolling surface was captured using a high-speed camera. Using the grid lines pre-drawn on the rolling surface can obtain the rolling trajectory of the test block, and then determine the stopping distance of the test block on the rolling surface, finally obtaining the initial rolling speed and corresponding stopping distance of the test block.

2.2. Determination of Rolling Friction Coefficients for Different Rolling Surface Materials

This paper mainly explores how rock shape affects its rolling distance. Nonetheless, as highlighted by Cui [19], rolling resistance is influenced by the test block's shape and the material properties of the rolling surface. Thus, in order to quantify how different rolling surface materials affect the rolling distance of rocks, it is essential to experimentally measure the rolling friction coefficients for different materials used in rolling.

For spherical test blocks, the rolling resistance due to shape effects can be neglected. Therefore, when assessing the impact of rolling surface materials on rolling distance, we can utilize the method introduced by Cui Tao [46] for calculating rolling friction coefficients. These experiments are performed with spherical test blocks, and the rolling friction coefficients on various rolling surface materials are determined from experimental data.

2.2.1. Experimental Setup

The experimental setup, depicted in Figure 5, includes the adjustment and installation of the rolling slope to ensure the flat and secure placement of materials. Coordinate grid paper and grid lines on the slope material are used for marking the positions of small spheres, while a velocity measurement device records their velocities on various rolling slopes.

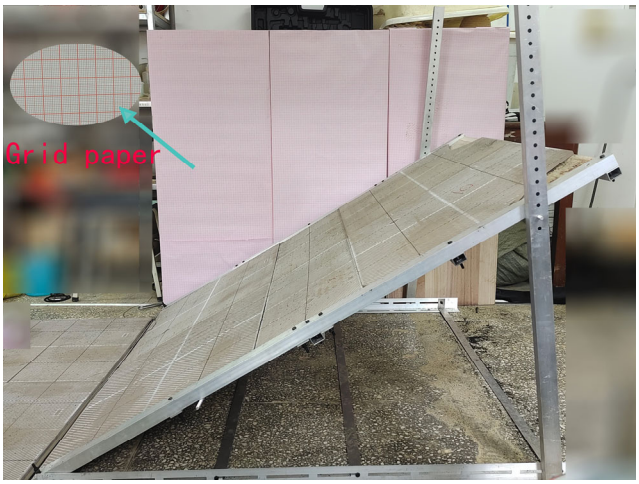

Figure 5. Experimental setup for determining material friction coefficients.

2.2.2. Experimental Procedure

Small spheres were positioned on rolling slopes with a consistent height of 45 cm and an incline angle θ. They were released from rest and allowed to slide down to the slope's base. Twelve distinct slope angles, spanning from 15° to 70°, were chosen for the experiments. Each type of rolling surface material underwent 12 repetitions (four for each sphere size, totaling 12 times), and the results were averaged to generate 12 datasets for each material.

3. Analysis of Experimental Results

3.1. Dispersion Analysis of Test Data

It was found during the test that the rolling trajectory of the test block had strong randomness, and the results obtained under the same conditions were not unique. Therefore, the average of multiple sets of test results obtained under the same conditions was taken as

the actual rolling distance of the test block under this condition, and the standard deviation between each set of data and the average value was calculated. However, considering the large difference in scale between the rolling distances of different shapes of test blocks, directly using the standard deviation could not accurately describe the dispersion of the test data. Therefore, in order to more accurately verify the reliability of the data from model tests, the ratio of the standard deviation to its corresponding mean value, known as the coefficient of variation, was used as a parameter that reflects the degree of dispersion of the test data. The test data of the test blocks rolling on different rolling surfaces were processed separately to obtain the corresponding coefficients of variation, as shown in Figures 6–8. The values in the error bars correspond to the standard deviations of the corresponding test blocks. The test data of test blocks with a coefficient of variation greater than 10% are shown in Table 3.

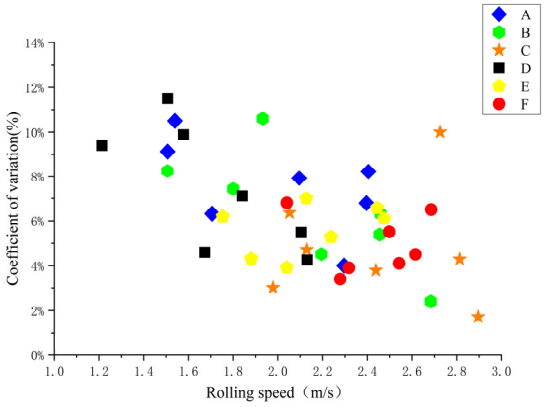

Figure 6. Coefficient of variation of rolling test results of test blocks on wooden boards.

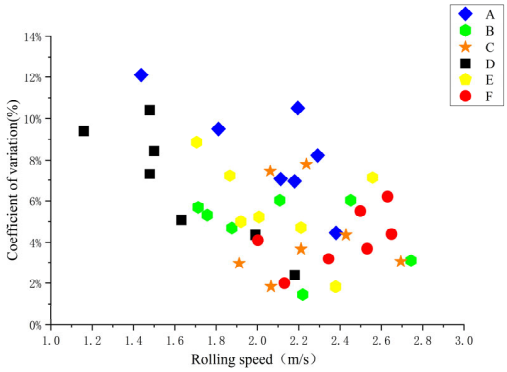

Figure 7. Coefficient of variation of rolling test results of test blocks on the back of ceramic tiles.

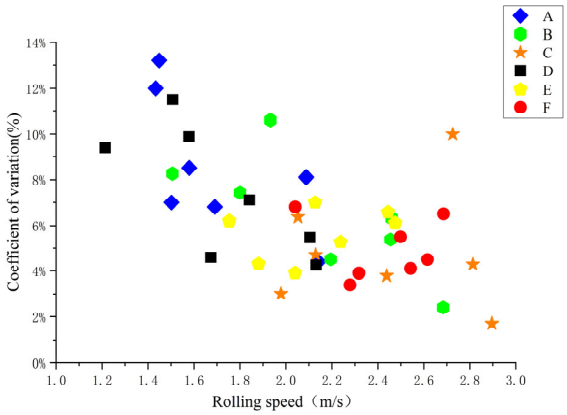

Figure 8. Coefficient of variation of rolling test results of test blocks on turf.

Table 3. Data sets with a coefficient of variation greater than 10% in the experimental results.

Rolling Surface Material	Test Block Number	Speed (m/s)	Test Rolling Distance (m)					Average	Standard Deviation	Coefficient of Variation (%)
			S_1	S_2	S_3	S_4	S_5			
Turf	A	1.54	0.220	0.276	0.278	0.245	0.218	0.247	0.026	10.5
	D	1.18	0.168	0.150	0.174	0.130	0.140	0.152	0.017	10.8
	D	1.87	0.344	0.352	0.380	0.437	0.455	0.394	0.045	11.4
Board	A	1.44	0.190	0.190	0.255	0.242	0.231	0.222	0.027	12.1
	A	2.20	0.430	0.531	0.410	0.523	0.450	0.469	0.049	10.5
	D	1.48	0.192	0.203	0.251	0.244	0.215	0.221	0.023	10.4
Back of ceramic tile board	A	1.43	0.166	0.157	0.194	0.212	0.210	0.188	0.022	12.0
	A	1.45	0.208	0.214	0.192	0.155	0.159	0.186	0.024	13.2
	B	1.93	0.595	0.466	0.489	0.536	0.612	0.540	0.057	10.6
	C	2.73	1.881	1.900	2.295	1.796	2.235	2.021	0.203	10.0
	D	1.51	0.226	0.185	0.192	0.241	0.183	0.205	0.024	11.5
	F	2.24	1.580	1.650	1.830	2.140	2.110	1.862	0.230	12.3
	A	1.54	0.220	0.276	0.278	0.245	0.218	0.247	0.026	10.5
	D	1.18	0.168	0.150	0.174	0.130	0.140	0.152	0.017	10.8
	D	1.87	0.344	0.352	0.380	0.437	0.455	0.394	0.045	11.4

From Table 3, the maximum coefficient of variation in the total test data is 13.2%, and the data with a coefficient of variation greater than 10% account for 9.5% of the total data. This indicates that the experimental error is well controlled, the quality of the model test is relatively reliable, and the experimental results can be used to analyze the influence of the shape of the test block on its rolling distance.

3.2. Relationship between Rock Shape and Rolling Distance

To delve deeper into how rock shape affects rolling distance, scatter plots were generated using experimental results. These plots depict the rolling distances of test blocks with various shapes on different rolling surface materials and at varying speeds, as displayed in the figures below.

Upon examination of Figures 9–11, a positive correlation between the rolling distance and the number of edges in the two-dimensional cross-section shape of the test block during rolling is evident. This discovery aligns with the conclusions reached by Ge et al. [47] through the utilization of rockfall software rockfall 5.0. In the case of test blocks rolling on a surface, if the rolling torque generated by kinetic energy is lower than the opposing rolling torque arising from gravity and the resistance attributed to the test block's shape and the characteristics of the rolling surface, the test block ceases to roll. The resisting rolling torque due to gravity relies on the test block's shape, as depicted in Figure 12. Owing to variations in shape, the side length of the cross-section shape of the twelve-edged prism F, oriented perpendicular to the rolling surface, is smaller than that of the four-edged prism D with the same volume. This implies that under identical conditions, test block F demands less force to surmount the rolling resistance than test block D, leading to a greater rolling distance for test block F. Consequently, it can be inferred that the number of edges in the two-dimensional cross-section shape of the test block, perpendicular to the rolling surface, exhibits a negative correlation with rolling resistance.

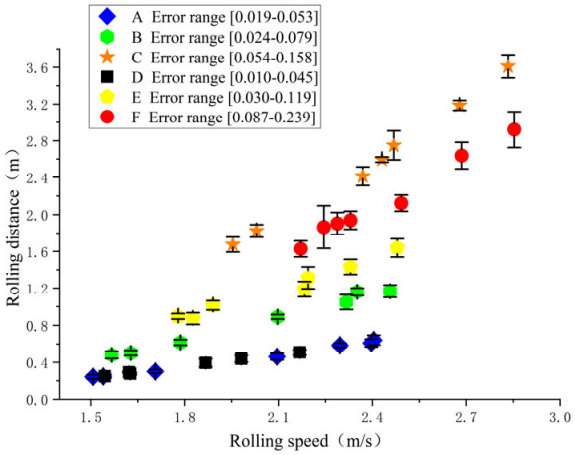

Figure 9. Experimental results of test blocks rolling on wood.

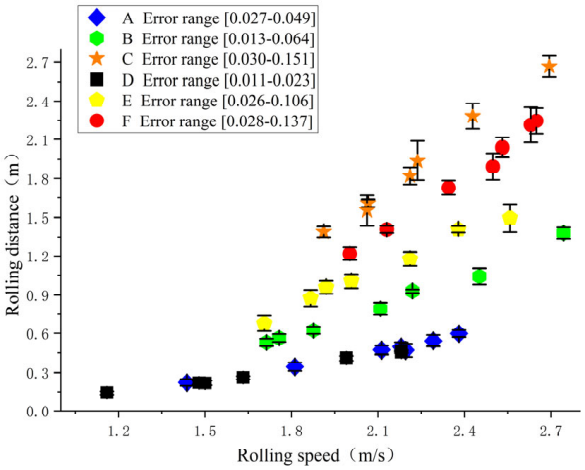

Figure 10. Experimental results of test blocks rolling on ceramic tile backing.

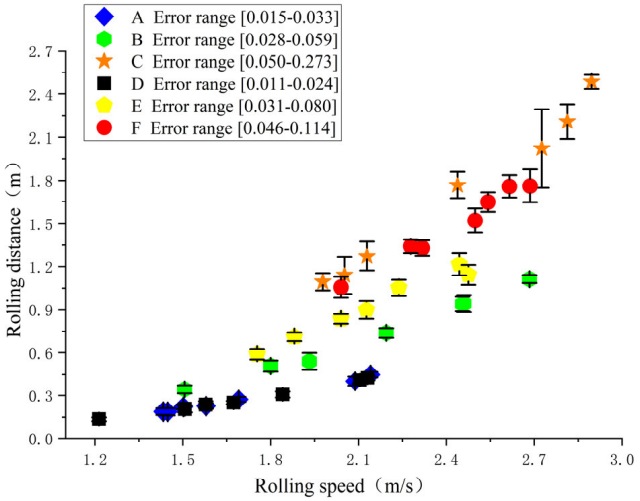

Figure 11. Experimental results of test blocks rolling on artificial turf.

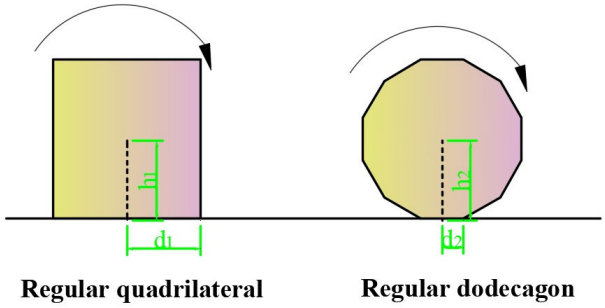

Figure 12. *RF* for different-shaped test blocks.

The rolling resistance dependent on the test block's shape is quantified by a coefficient known as the delayed rolling factor (*RF*). *RF* is defined as the ratio of the distance from the rolling stone's center of mass to the ground (*h*) to the distance from the instantaneous center to the center of mass and perpendicular to the ground (*d*):

$$RF = \frac{d}{h} \tag{1}$$

Variations in shape lead to distinct behaviors during rolling. In the case of cubic test block A, where the long and short axes have equal lengths, the rolling resistance when rolling about these axes is identical. Consequently, there is a greater potential for offset and axis transition during rolling. The occurrence of offset or axis transition implies that the test block must overcome a sudden increase in rolling resistance during the transition, as illustrated in Figure 13. This substantially depletes the rolling kinetic energy of test block A, leading to a reduction in its rolling distance and an increase in offset distance. Experimental observations revealed that test blocks with a length-to-width ratio exceeding two rarely undergo axis transition during rolling. For instance, test blocks B and C exhibit slight lateral swaying during rolling, but due to their rotational inertia, they exhibit stability, reducing the likelihood of toppling or altering their rolling axis. At very low rolling speeds, when rotational inertia is insufficient to maintain stability, test blocks may tilt and come to a halt. In the cases of test blocks D, E, and F, their rolling process involves a substantial ground contact area, resulting in significant axis transition and increased post-transition rolling resistance compared to initial rolling resistance. Consequently, in the absence of collisions, they tend to roll about the axis with lower rolling resistance, consistent with the findings of Azzoni [48].

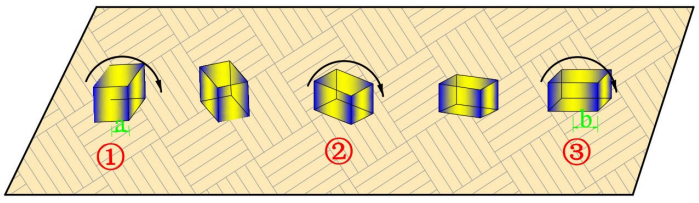

Figure 13. Variation of δ during axis transition of the test block.

Certain test blocks that undergo offset exhibit varying degrees of reduced rolling distances. In addition to the potential for test block A to undergo a change in rolling axis during offset, which could elevate rolling resistance, the remaining test blocks experience kinetic energy loss due to offset. This occurs because, during the offset process, an angle exists between the direction of rolling kinetic energy and the direction of motion, as depicted in Figure 14. This impedes the complete utilization of the test block's kinetic energy, leading to a decrease in its rolling distance.

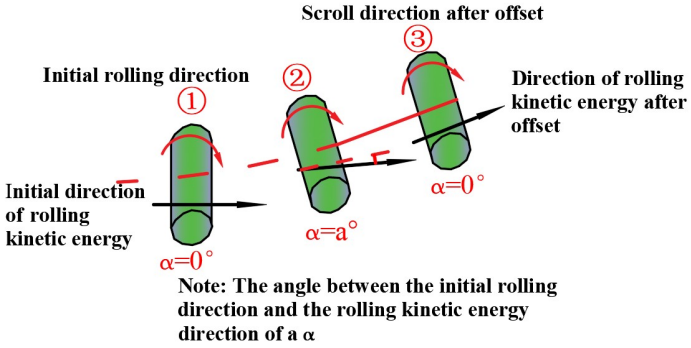

Figure 14. Variation of the angle between the direction of rolling and rolling kinetic energy before and after offset.

If the offset angle remains constant, the influence of rotational inertia causes the angle between the rolling kinetic energy direction and motion direction to vanish upon offset completion, as illustrated in Figure 15a. When the offset angle continuously varies, the angle between the rolling kinetic energy direction and motion direction oscillates between 0° and the current offset angle during each occurrence, as depicted in Figure 15b.

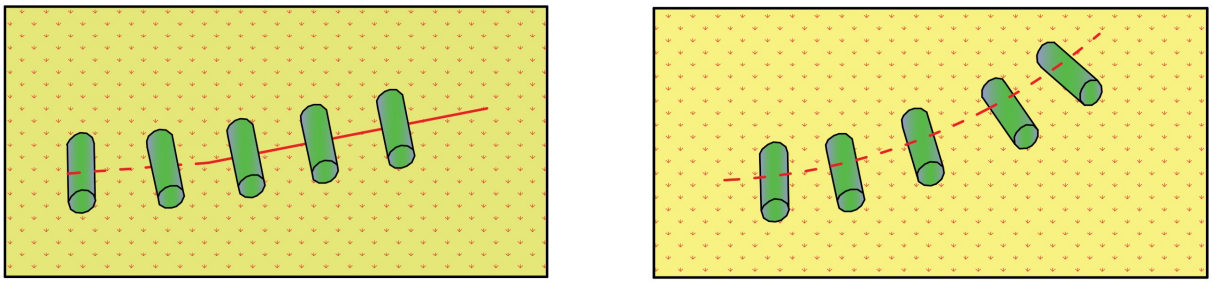

(**a**) (**b**)

Figure 15. Variation of δ during axis transition of the test block: (**a**) the offset angle no longer changes; (**b**) the offset angle is constantly changing.

Figure 16 illustrates the stopping positions of test blocks A, B, and E as they roll on rolling surfaces made of different materials with an initial velocity of 2.2 m/s, and as their velocities reach zero.

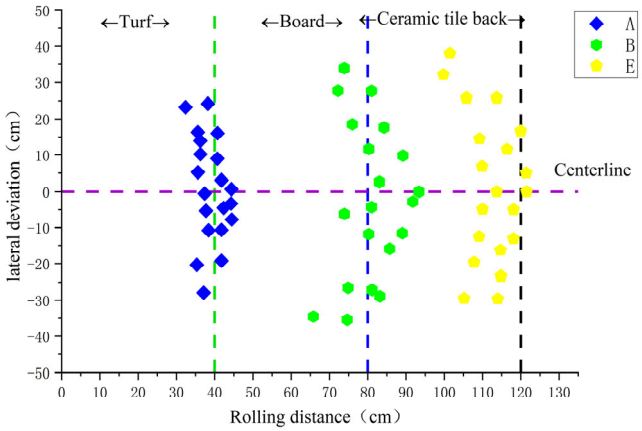

Figure 16. Experimental results of test blocks rolling on composite ground materials. (The green dashed line represents the boundary between the turf and the wooden board, the blue dashed line represents the boundary between the wooden board and the back of the ceramic tile board, and the black dashed line represents the boundary between the back of the ceramic tile board and the ground).

The results indicate that, on flat ground, the primary determinant of rolling distance is the test block shape, whereas the hardness of the ground material has a comparatively limited effect. Observation of rolling characteristics during the test blocks' transition between two distinct materials reveals that varying material hardness leads to uneven deformation of the rolling surface during the transition. During the transition from a highly deforming surface to a less deforming one, the test block encounters a "step" created by the deformation difference between the two materials. The height of this "step" is determined by the hardness contrast between the two adjacent materials, as depicted in Figure 17. The presence of the "step" influences the test block rolling distance. A relatively low "step" is less likely to hinder the test block during rolling, resulting in minimal disruption. However, a "step" of a certain height can lead to collisions with the test block, diminishing its rolling distance or even causing it to cease rolling immediately post-collision. In instances where adjacent materials exhibit similar hardness at the boundary, the obstruction at the boundary is lower in height and has a minimal impact on the test block rolling.

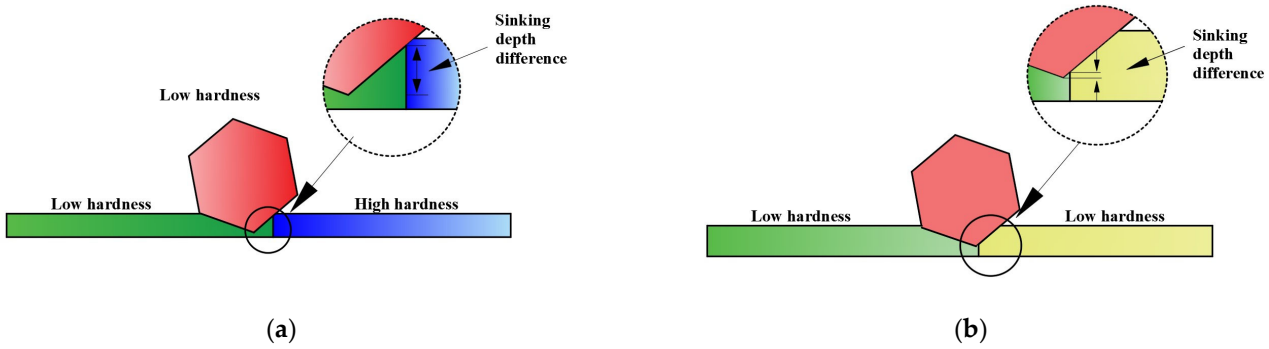

Figure 17. "Steps" formed on different material boundaries by the test blocks: (**a**) the test block rolls from low hardness to high hardness; (**b**) the test block rolls from high hardness to low hardness.

3.3. Calculation of Rolling Friction Coefficients for Different Slope Materials

When a ball of mass m rolls uniformly on various rolling materials, the magnitude of its rolling resistance depends on the level of deformation upon contact with the rolling surface, as depicted in Figure 18a. In the ideal scenario, with no deformation occurring in either the ball or the rolling surface, the ball's RF coefficient is 0. When a horizontal rightward force F is applied to the ball, it will continue rolling uniformly until it exits the rolling surface unless an additional external force is exerted.

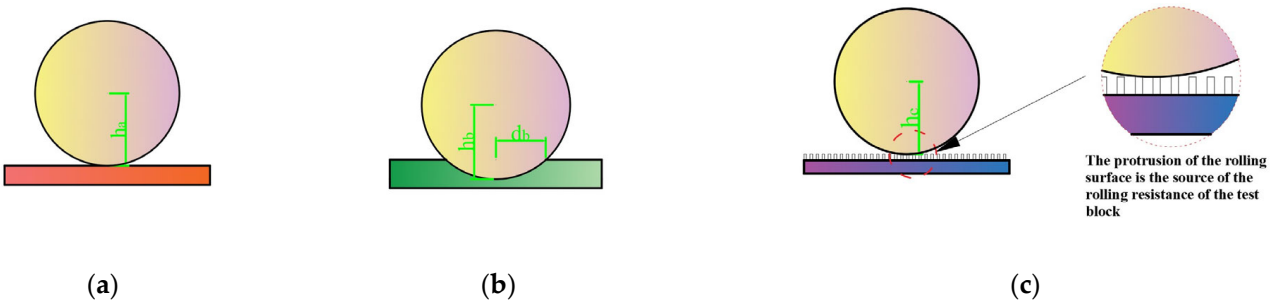

Figure 18. Deformation of spherical test blocks rolling on different surfaces: (**a**) no deformation on the test block and rolling surface; (**b**) the angle at which the deviation occurs constantly changes; (**c**) the rolling surface is flat but has slight undulations.

Nonetheless, for the balls depicted in Figure 18b,c, their rolling resistance is influenced by the properties of the rolling surface materials.

When the ball rolls uniformly under the influence of an external force F, it adheres to the following equilibrium formula:

$$Fr\cos\alpha - Gd = 0 \tag{2}$$

where

d—the distance from the instant center to the center of mass of the ball when it rolls on the rolling surface;
r—the radius of the ball;
G—the mass of the ball;
α—the angle formed by the vertical line through the center of mass of the ball and the line from the instant center to the center of mass of the ball.

When the ball rolls uniformly on the rolling surface, the small angle α between the vertical line through the ball's center of mass and the line from the instant center to the center of mass results in cosα equating to 1. Consequently, Formula (2) simplifies to:

$$F = \frac{d}{r}mg \tag{3}$$

In this scenario, the force F acting on the ball aligns with the rolling resistance F_f:

$$F_f = \frac{d}{r}mg \tag{4}$$

Consequently, the work performed by the frictional force arising from the rolling material's characteristics during the ball's descent on the sloped surface can be computed as:

$$W_f = F_f L = \frac{d}{r}mg\cos\theta L \tag{5}$$

where

L—the rolling distance of the ball on the slope surface;
θ—the slope.

In accordance with the law of energy conservation, it is apparent that the overall energy of the ball rolling on the sloped surface is dictated by the initial release height, specifically the gravitational potential energy E_h. Consequently, when the ball descends on the sloped surface, Equation (5) can be derived as:

$$C_f = \frac{W_f}{E_h} = \frac{E_h - \frac{1}{2}mv^2}{E_h} = \frac{d}{r}\cot\theta \tag{6}$$

where

C_f—linearly related to the slope's tangent, with the slope-dependent rolling friction coefficient μ;
v—the rolling velocity of the ball on the slope surface (m/s).

The data collected during the rolling of spherical balls on various slopes were systematically analyzed. Linear regression was employed to determine the relationship between C_f and cotθ, as depicted in Figures 19–21. This analysis yielded the rolling friction coefficients μ for balls of different masses and sizes on different materials. The resulting rolling friction coefficients μ_1, μ_2, and μ_3 for the balls rolling on wood, ceramic tile, and artificial turf were found to be 0.07, 0.09, and 0.13, respectively.

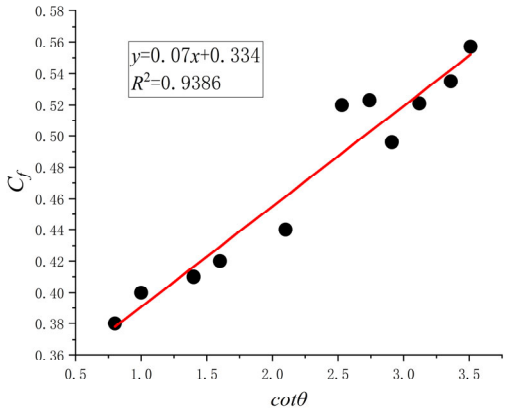

Figure 19. Rolling friction coefficient between spherical ball and wooden board.

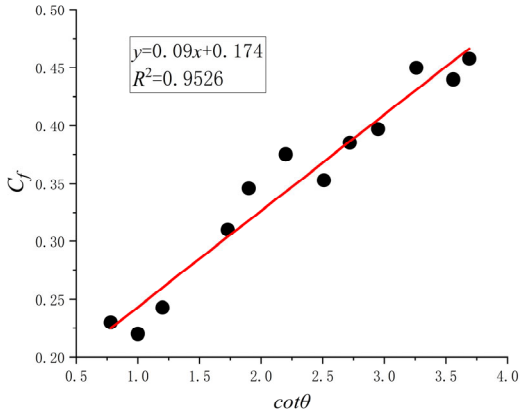

Figure 20. Rolling friction coefficient between spherical ball and ceramic tile back.

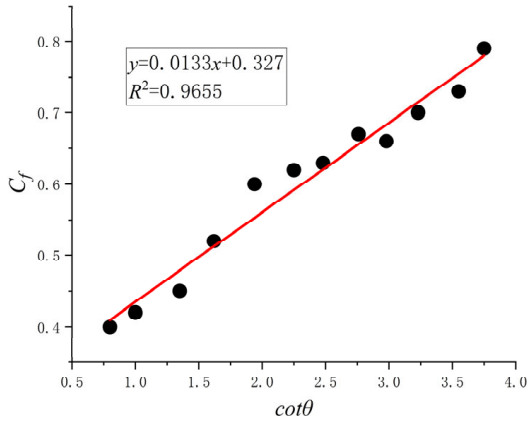

Figure 21. Rolling friction coefficient between spherical ball and artificial turf.

4. Theoretical Analysis

Model Derivation

Analysis of the experimental results regarding the rolling distance of the test blocks clearly indicates that shape is the most significant influencing factor. This is primarily associated with the two-dimensional cross-sectional shape of the rolling test block. The ease of test block rolling can be characterized by the previously introduced rolling resistance coefficient *RF*. However, *RF* alone cannot quantify the effect of stone shape on the rolling stopping distance. In order to quantify the impact of stone shape on the rolling stopping distance, an analysis from a statics perspective is performed, to investigate the connection

between the test block's shape and rolling resistance. Furthermore, two concepts related to rolling, namely rolling resistance and rolling resistance arm, are introduced.

When a stone departs from the slope with a specific initial velocity and rolls on flat ground with varying properties until its speed diminishes to zero, it is assumed that no collisions or ruptures take place during the rolling. The resistance encountered by the stone during the rolling process arises from both its own shape and the deformation that transpires during its interaction with the rolling surface. In the course of the rolling process, the torque that impedes rolling, stemming from the stone's shape, is termed rolling resistance. The lever arm responsible for creating the rolling resistance torque is denoted as the rolling resistance arm.

In the case of polygonal test blocks in contact with the ground, the length of their rolling resistance arm δ is contingent upon the contact configuration between the test block and the ground. A shorter length of contact edges with the ground translates to a smaller rolling resistance that must be overcome. As illustrated in Figure 22, for a pentagonal test block with an edge length of a in contact with the ground, the maximum rolling resistance arm δ equals a/2. As the contact length between the test block and the ground diminishes, approaching a circular configuration, the rolling resistance arm δ diminishes to zero, resulting in zero rolling resistance for the test block.

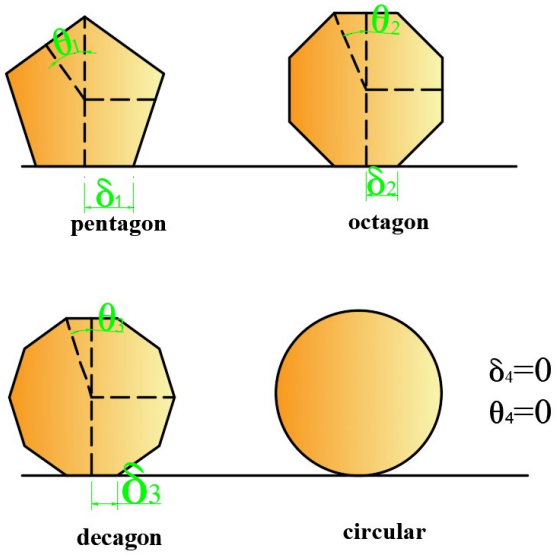

Figure 22. Relationship between the number of edges in the two-dimensional shape of the test block and rolling resistance.

Based on the preceding analysis, it becomes apparent that the magnitude of rolling resistance encountered by a stone is governed by the fundamental conditions of its interaction with the ground, particularly the rolling resistance arm δ. Hence, when assessing the influence of stone shape on its rolling distance, it is imperative to take into account the stone's cross-sectional shape and to choose parameters that can effectively quantify its impact on rolling. Among these parameters, for a more precise selection of characteristic parameters defining the stone's shape, it is recommended to conduct a comprehensive analysis utilizing three categories of scales conventionally employed for characterizing block morphology [49], as illustrated in Figure 23. The areas of the minimum circumscribed circle and the two-dimensional cross-section perpendicular to the ground capture both the local and global aspects of falling rock shapes, offering a robust representation of the stone's shape characteristics.

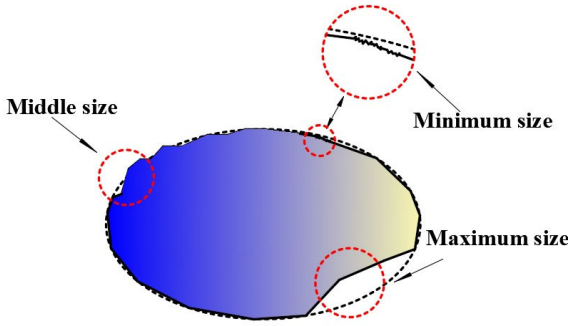

Figure 23. Schematic of three categories of scales for rock blocks.

Therefore, in this paper, the difference between the area of the two-dimensional cross-section of the stone perpendicular to the ground during its rolling and the area of its minimum circumscribed circle is divided by the area of the minimum circumscribed circle. This ratio, which quantifies the rolling resistance dependent on the stone's shape, is referred to as the rolling resistance coefficient ψ:

$$\psi = \frac{u_1 - u_2}{u_1} \tag{7}$$

where

u_1—the area of the smallest circumscribed circle among the maximum two-dimensional cross-sectional shapes of the stone perpendicular to the slope;
u_2—the area of the maximum two-dimensional cross-sectional shape of the stone perpendicular to the slope.

As mentioned earlier, the rolling resistance of the stone is influenced by both its shape and the deformation that transpires on the rolling surface as the stone moves. To calculate the overall rolling friction coefficient, we must take into account rolling resistance coefficients from two perspectives: the properties of the rolling surface in contact with the stone and the geometric shape of the stone. The rolling friction coefficient μ for the rolling surface material employed in this experiment is determined through experimentation. Meanwhile, the rolling friction coefficient ψ, stemming from the geometric shape of the stone, is computed using Equation (7). The rolling resistance f of the test block during rolling is subsequently expressed as:

$$f = (\psi + \mu)N \tag{8}$$

where

μ—rolling friction coefficient originating from ground characteristics, determined experimentally in this paper.

When the stone is in motion on the ground, a kinematic analysis of the block depicted in Figure 24 produces the following equations:

$$mg\sin\theta - f = ma \tag{9}$$

$$a = g[\sin\theta - (\psi + \mu)\cos\theta] \tag{10}$$

$$v^2 - v_0^2 = 2as \tag{11}$$

$$v = \sqrt{v_0^2 + 2as} = \sqrt{v_0^2 + 2g(\sin\theta - (\psi + \mu)\cos\theta)s} \tag{12}$$

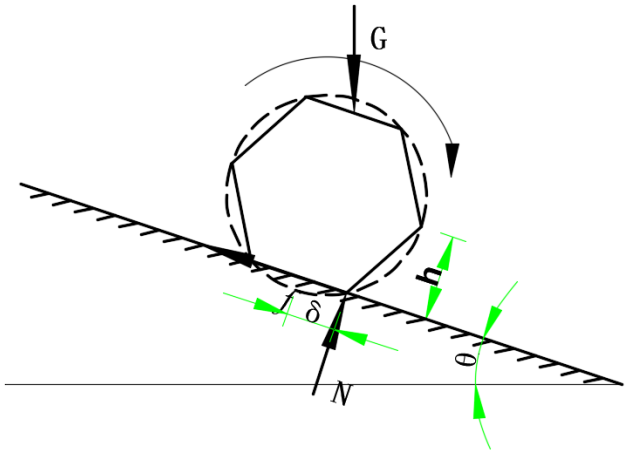

Figure 24. Rolling force diagram of test block slope.

The rolling distance S of the stone on the ground, when it has reached a slope angle of 0°, is given by Equation (13):

$$S = \frac{v^2}{2g(\psi + \mu)} \tag{13}$$

During the analysis of the experimental data, it became evident that test blocks with a relatively small aspect ratio (the ratio of the long axis to the short axis) experienced comparable rolling resistance when rolling along different axes. This frequently resulted in deviations or alterations in the rolling axis, leading to a substantial decrease in rolling distance. Consequently, for test blocks with an aspect ratio below two, it becomes imperative to account for their rolling stopping distance when performing calculations for various rolling axes. This guarantees that, in the event of deviations or alterations in the test block's rotational axis, its rolling stopping distance remains consistent with the calculated range.

The rolling stopping distance for test blocks with different axes can be determined utilizing the following equations:

$$S_{\max} = \frac{v^2}{2g(\psi_{\max} + \mu)} \tag{14}$$

$$S_{\min} = \frac{v^2}{2g(\psi_{\min} + \mu)} \tag{15}$$

where

$S_{\max}$—maximum rolling distance when rolling around the long axis;
$S_{\min}$—minimum rolling distance when rolling around the short axis.

When the test block rolls on rolling surfaces consisting of multiple materials and has the potential to transition between them, the total rolling distance S can be calculated using the following formulas:

When $S_1 < S$:

$$S = S_1 + \frac{v_0^2 - 2g(\psi_{max} + \mu_1)S_1}{2g(\psi_{max} + \mu_2)} \tag{16}$$

When $S_1 + S_2 < S$:

$$S = \frac{v_0^2 - 2g(\psi_{max} + \mu_1)S_1 - 2g(\psi_{max} + \mu_2)S_2}{2g(\psi_{max} + \mu_3)} + S_1 + S_2 \tag{17}$$

where

S_1—rolling distance on the first type of rolling surface;
S_2—rolling distance on the second type of rolling surface;

S—total rolling distance;
S_n—rolling distance on different ground features.

For test blocks with an aspect ratio below two, when defining the rolling range, you can initially compute the deviation angle β using Hu's method [50]. Subsequently, guided by the calculated deviation angle, you can ascertain the maximum rolling distance free from deviations, and the maximum rolling distance with deviations, for rolling along both the long and short axes. Connecting the determined endpoints forms a sector-shaped rolling range, as depicted in Figure 25a. For test blocks with an aspect ratio below two, it is sufficient to calculate the rolling stopping distance when rolling along the axis with lower rolling resistance and subsequently connect the computed endpoints, as illustrated in Figure 25b.

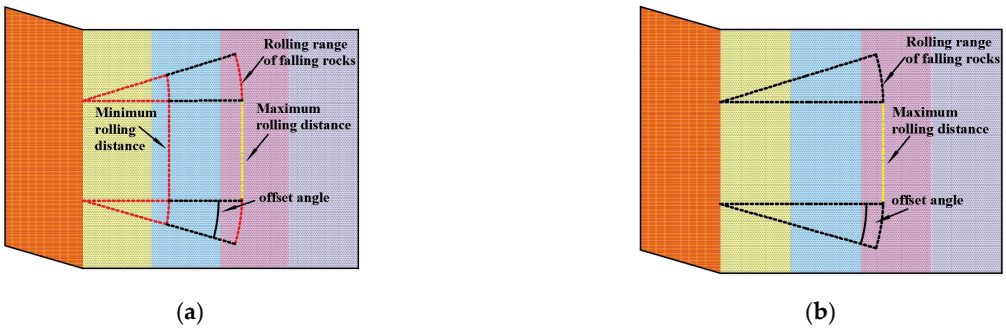

(**a**) (**b**)

Figure 25. Determination of rolling distance for falling rocks: (**a**) rolling range for test blocks with aspect ratio < 2, rolling around long and short axes with deviation; (**b**) rolling range for test blocks with aspect ratio < 2, rolling around axis with lower rolling resistance. In the figure, orange represents the release slope of the test block, yellow is artificial turf, blue is wood, light purple is the back of the tile board, and gray is the ground.

5. Experimental Results and Theoretical Formula Calculation Comparison

5.1. Comparison Analysis for Single Slope Characteristics

To validate the precision of the calculation formulas, we compared the experimental results of test blocks with diverse shapes rolling on wooden boards, the backside of ceramic tiles, and artificial turf to the outcomes derived from the formulas. These comparisons are illustrated in Figures 26–28.

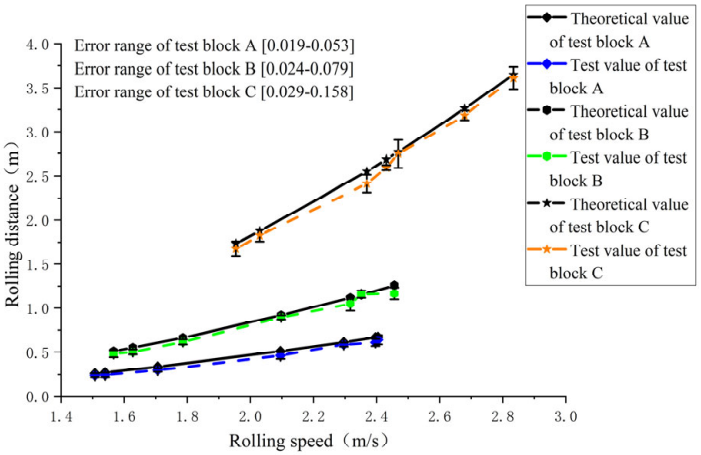

Figure 26. Experimental and calculated comparison for test blocks rolling on wooden boards.

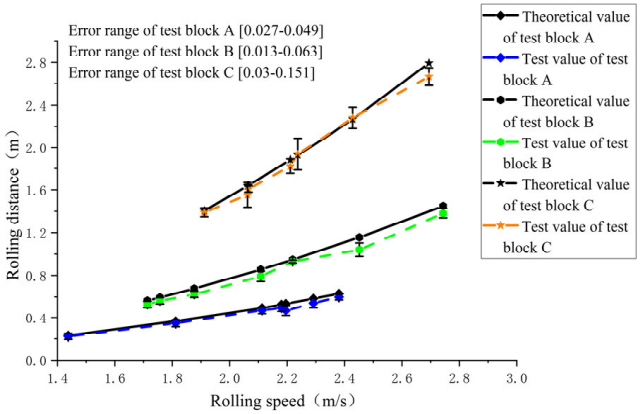

Figure 27. Experimental and calculated comparison for test blocks rolling on the backside of ceramic tiles.

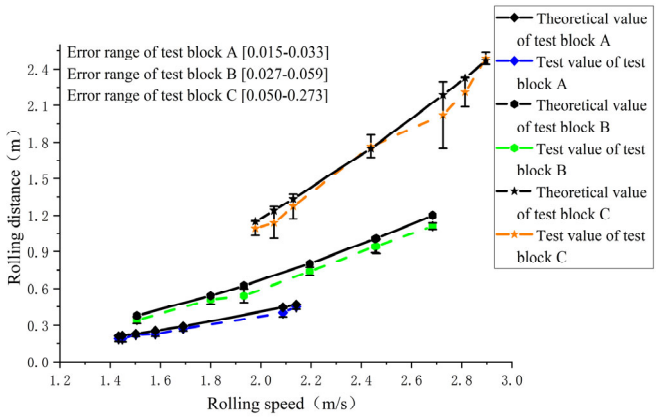

Figure 28. Experimental and calculated comparison for test blocks rolling on artificial turf.

The discrepancies between the computed results obtained from the formulas and the experimental measurements for test blocks rolling on various rolling surface materials were as follows: 5.7% for wooden boards, 5.2% for the backside of ceramic tiles, and 7.5% for artificial turf.

The relatively substantial error observed in the case of artificial turf can be ascribed to its lower hardness in comparison to the test blocks, leading to considerable surface deformation while rolling. Moreover, the uneven distribution of hardness and surface irregularities on the turf heightened the probability of test block deviations and energy dissipation during rolling, consequently resulting in a greater disparity between the computed and experimental outcomes.

In contrast, wooden boards, which exhibited lower hardness than the test blocks, induced minimal surface deformation during the rolling process due to their high surface flatness. This minimized the likelihood of test block deviations and, as a result, diminished the error between the experimental and computed results.

In the case of the backside of ceramic tiles, possessing hardness akin to that of the test blocks, the surface displayed shallow, fine-striped grooves, which were significantly smaller in dimension compared to the test block size. Consequently, the rolling behavior of the test block on the backside of ceramic tiles was essentially tantamount to rolling on a flat surface. Moreover, the minimal deformation of the rolling surface, attributable to its higher hardness, led to the smallest discrepancy between the experimental and computed values.

The average discrepancies for test blocks A, B, and C were determined to be 8.4%, 7.1%, and 3%, correspondingly. In the analysis of test block A's shape characteristics, it was observed that the equal lengths of its long and short rolling axes resulted in consistent challenges in overcoming rolling resistance during the rolling process. Nevertheless, this

also heightened the probability of test block A altering its rolling axis during the rolling, resulting in deviation as it transitioned from the slope to the ground. The block retained its rolling posture on the ground as it departed from the slope, which induced axis variation and deviation. This phenomenon contributed to escalated rolling resistance, a reduction in the rolling distance, and ultimately led to calculated values surpassing experimental values.

In the case of test block B, an increase in the number of sides in its cross-sectional shape resulted in a reduction in rolling resistance caused by its shape. Moreover, a notable disparity in resistance was observed when rolling around the long and short axes. Additionally, the preservation of its original rolling axis during the rolling process, enabled by the constraint of rotational inertia, diminished the probability of axis variation. As a result, the observed error was mainly attributable to block deviation during the rolling process.

Test block C demonstrated comparable rolling characteristics to test block B when on the ground. Nevertheless, its shape-induced rolling resistance was minimal, leading to reduced chances and magnitude of deviation during rolling. Typically, during experiments, test block C consistently rolled in a straight line, yielding longer rolling distances and minimal discrepancies between calculated and experimental values.

For blocks with a length-to-width ratio of less than 2, we took into account the potential for axis variation during rolling. The cross-sectional shape corresponding to the longest and shortest dimensions was employed to compute the block's maximum and minimum rolling distances. Compare the actual rolling distance of test blocks D, E, and F on the rolling surface with different initial speeds over 14 trials with the calculated maximum and minimum rolling distances and the test values, as depicted in Figures 29–31.

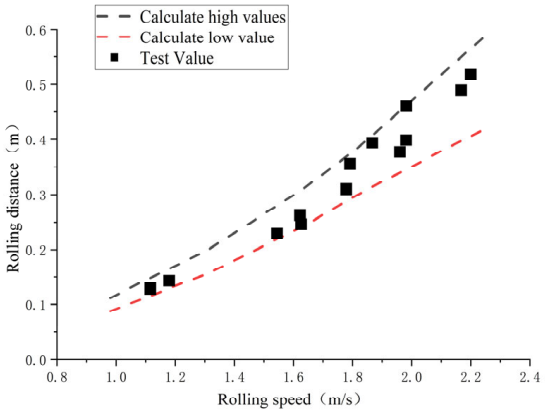

Figure 29. Comparison between experimental and calculated values for test block D.

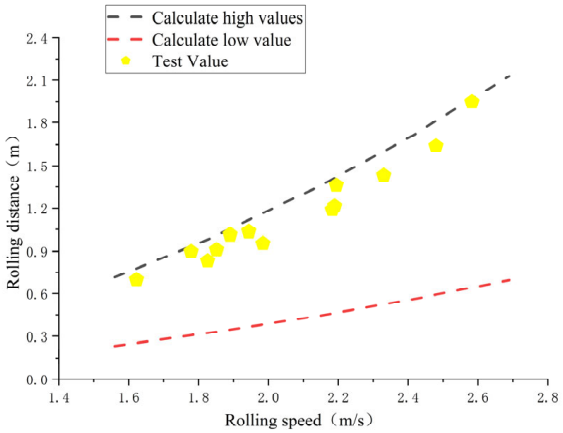

Figure 30. Comparison between experimental and calculated values for test block E.

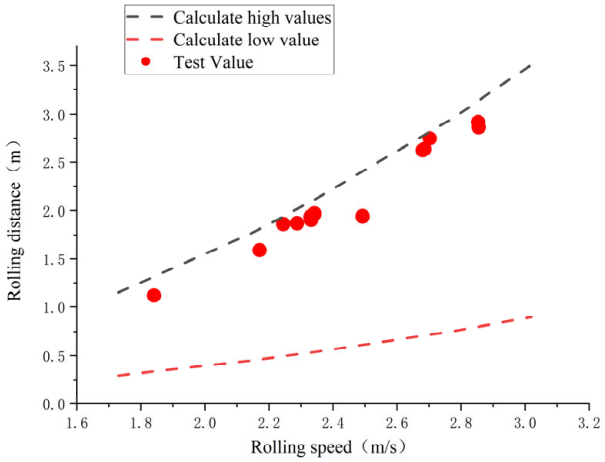

Figure 31. Comparison between experimental and calculated values for test block F.

In Figure 29, it is evident that Test Block D's rolling distance during the experiment tended to align with the lower calculated value. This trend was observed because blocks with a larger rolling resistance, stemming from their maximum two-dimensional shape perpendicular to the rolling surface, consumed more kinetic energy during the deviation process. This resulted in a final rolling distance that fell below the lower calculated value. In contrast, test blocks E and F, with lower rolling resistance, exhibited smaller deviation angles during rolling. Furthermore, these blocks often maintained straight-line rolling post-deviation, preventing energy loss. Consequently, the experimental values for these blocks tended to approach the higher calculated value.

5.2. Comparison Analysis for Composite Slope Characteristics

To confirm the suitability of the formula for calculating composite ground materials, we assessed the rolling range of test blocks. This assessment considered their shape characteristics, deviation, and the velocity at which they left the slope. The test results of rolling the test block on the rolling surface over 20 trials at an initial velocity of 2.2 m/s are directly plotted on the composite ground. The points in the figure correspond to the final stop position of the test block as shown in Figures 32–34.

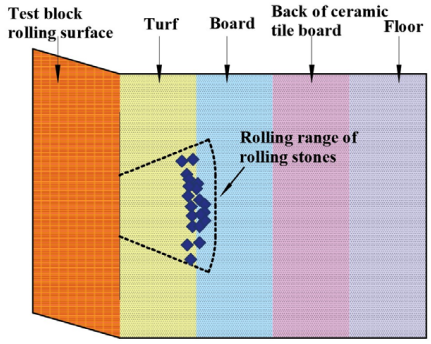

Figure 32. Rolling behavior of test block A on composite ground.

In Figure 32, test block A's rolling range consistently fell within the calculated parameters, with rolling distances slightly shorter than the calculated values. Notably, 60% of the test blocks did not transition between two types of ground materials, and 30% of these came to an immediate halt after crossing the boundary. This can be attributed to the elevated rolling resistance of the test blocks. As they neared the "step", their rolling speed had considerably decreased. The minor ground irregularities could easily impede their progress, leading to a subset of test blocks remaining at the boundary.

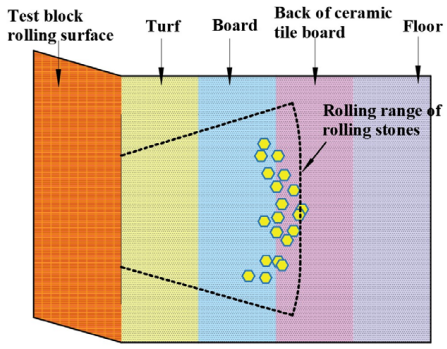

Figure 33. Rolling behavior of test block B on composite ground.

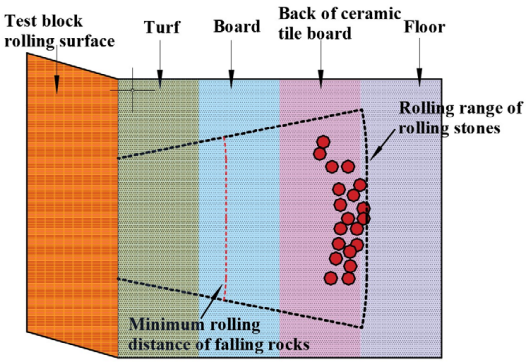

Figure 34. Rolling behavior of test block F on composite ground.

Test block B, characterized by reduced rolling resistance, retained a more significant amount of rolling kinetic energy as it approached the "step". In this scenario, 65% of the test blocks successfully traversed the boundary between two ground materials. For the subset that did not cross, their average deviation was 2.1 times greater than those that did, as indicated in Figure 33. The introduction of the "step" led to deviations in test block B's path after transitioning to new material, resulting in relatively substantial deviations. Nevertheless, the rolling range after deviation remained consistent with the calculated parameters.

Test block F, which encountered three types of ground materials, experienced the least rolling resistance due to its shape and the higher circularity of its two-dimensional cross-sectional shape. This enhanced its ability to navigate different materials. Remarkably, all test blocks successfully surpassed the minimum rolling distance, as illustrated in Figure 34. In comparison to test blocks A and B, their lateral deviation was notably smaller, averaging a mere 23%. This reduction in deviation minimized the energy dissipation during rolling, enabling the test blocks to swiftly traverse the boundaries between various ground materials. Consequently, the impact of the ground material on the test blocks during rolling was relatively minor, resulting in a reduced margin of error between calculated and experimental values.

6. Conclusions and Prospects

6.1. Conclusions

1. The shape of rolling stones is a critical factor that impacts rolling distance, and it is associated with the number of edges in the stone's two-dimensional cross-section perpendicular to the rolling surface. We can quantify the level of difficulty in stone rolling using the *RF* coefficient introduced in this study.
2. Deviations or alterations in the rolling axis while a stone is rolling will influence the rolling distance. The degree of this impact is determined by the magnitude of

variation in the deviation angle, with greater variations leading to increased energy consumption.

3. When stones roll on composite ground with varying hardness on each side, the existence of "steps" created by differences in hardness can result in collisions or deviations at the boundary line. The degree of this impact relies on the size ratio between the stone and the "step". A greater ratio leads to a reduced impact, while a smaller ratio has the opposite effect.
4. Based on experimental data, the influence mechanism of shape on rolling stone distance was analyzed. A parameter quantifying the impact of stone shape on rolling distance was proposed and introduced into kinematic formulas. This led to rolling distance calculation formulas for stones of different shapes on different types of ground. Validation using experimental data showed that the errors between calculated and experimental values were small. It was also noted that energy consumption resulting from stone deviation and changes in the rolling axis during rolling reduced the rolling distance.
5. By using the proposed formulas and considering the deviation of stones with different shapes, the influence range of stones with different shapes rolling at different speeds can be plotted. Model tests were conducted for validation. However, the reduction in the actual terrain and geomorphology in natural rockfall disasters in model tests is limited, and only some factors that affect the rolling distance of rock blocks can be considered. It is impossible to completely replicate the natural characteristics of mountainous terrain. Therefore, after on-site testing verification, these findings can serve as a reference for the assessment of rolling stone danger zones and protection design.

6.2. Prospects

This study primarily concentrated on understanding how the shape of stones influences their rolling distance. It also proposed calculation formulas suitable for determining the rolling distances of test blocks on flat terrain. However, it did not address scenarios involving potential stone collisions or rebounds during motion. When stones roll on composite ground with significantly varying hardness levels, quantifying the impact of "steps" created by these differences on stone rolling distance becomes complex. The study solely considered the stone's shape and the properties of the rolling surface. In the future, it should encompass multiple factors influencing rolling distance, offering calculation formulas that account for various variables. This would enhance the versatility of the formulas.

Author Contributions: Conceptualization, F.L.; methodology, G.S.; software, N.H.; validation, N.H.; formal analysis, B.Y.; investigation, G.S.; resources, B.Y.; data curation, F.L.; writing—original draft preparation, N.H.; writing—review and editing, F.L.; visualization, N.H.; supervision, B.Y.; project administration, G.S.; funding acquisition, G.S. All authors have read and agreed to the published version of the manuscript.

Funding: The work was supported by the Natural Science Foundation of Guangxi, China (No. 2020GXNSFAA297078) and Guilin University of Technology Research Initiation Fund (GUTQDJJ2003031).

Institutional Review Board Statement: Not applicable.

Data Availability Statement: The data used to support the findings of this study are available from the corresponding author upon request.

Acknowledgments: Thanks to Yong-gen for his help in visualizing this paper.

Conflicts of Interest: The authors declare that they have no known competing financial interests or personal relationships that could have appeared to influence the work reported in this paper.

References

1. Luo, G.; Cheng, Q.G.; Shen, W.G. Research Status and Development Trend of the High-Altitude Extremely-Energetic Rockfalls. *Earth Sci.* **2022**, *47*, 913–934.

2. Zhang, Y.H.; Zhang, M.X.; Chen, Q.; Luo, K.J. Kinematics analysis for calculating distance of rockfalls on typical loose media slope. *J. Shanghai Univ. (Nat. Sci. Ed.)* **2017**, *23*, 949–960.
3. Frattini, P.; Crosta, G.B.; Agliardi, F. 22-Rockfall characterization and modeling. In *Landslides: Types, Mechanisms and Modeling*; Cambridge University Press: Cambridge, UK, 2012; pp. 267–281.
4. Leine, R.I.; Schweizer, A.; Christen, M.; Glover, J.; Bartelt, P.; Gerber, W. Simulation of rockfall trajectories with consideration of rock shape. *Multibody Syst. Dyn.* **2014**, *32*, 241–271. [CrossRef]
5. Vishal, V.; Siddique, T.; Purohit, R.; Phophliya, M.K.; Pradhan, S.P. Hazard assessment in rockfall-prone Himalayan slopes along National Highway-58, India: Rating and simulation. *Nat. Hazards* **2017**, *85*, 487–503. [CrossRef]
6. Sengani, F.; Mulenga, F. An improved hazard assessment chart for rock falls in near vertical blocky rock environments. *Environ. Earth Sci.* **2021**, *80*, 647. [CrossRef]
7. Moos, C.; Dorren, L.; Stoffel, M. Quantifying the effect of forests on frequency and intensity of rockfalls. *Nat. Hazards Earth Syst. Sci.* **2017**, *17*, 291–304. [CrossRef]
8. Yan, P.; Zhang, J.; Kong, X.; Fang, Q. Numerical simulation of rockfall trajectory with consideration of arbitrary shapes of falling rocks and terrain. *Comput. Geotech.* **2020**, *122*, 103511. [CrossRef]
9. Shirzadi, A.; Saro, L.; Joo, O.H.; Chapi, K. A GIS-based logistic regression model in rock-fall susceptibility mapping along a mountainous road: Salavat Abad case study, Kurdistan, Iran. *Nat. Hazards* **2012**, *64*, 1639–1656. [CrossRef]
10. Zhang, Y.; Zhang, J.; Wang, Q. Scene analysis of landslide geoscience and characterization of scene evolution. *Acta Geophys.* **2023**, *71*, 1539–1564. [CrossRef]
11. Perret, S.; Dolf, F.; Kienholz, H. Rockfalls into forests: Analysis and simulation of rockfall trajectories—Considerations with respect to mountainous forests in Switzerland. *Landslides* **2004**, *1*, 123–130. [CrossRef]
12. Bourrier, F.; Berger, F.; Tardif, P.; Dorren, L.; Hungr, O. Rockfall rebound: Comparison of detailed field experiments and al-ternative modelling approaches. *Earth Surf. Process. Landf.* **2012**, *37*, 656–665. [CrossRef]
13. Zhu, C.; He, M.-C.; Karakus, M.; Zhang, X.-H.; Guo, Z. The collision experiment between rolling stones of different shapes and protective cushion in open-pit mines. *J. Mt. Sci.* **2021**, *18*, 1391–1403. [CrossRef]
14. Gao, G.; Meguid, M.A. On the role of sphericity of falling rock clusters—Insights from experimental and numerical investigations. *Landslides* **2018**, *15*, 219–232. [CrossRef]
15. Kim, D.H.; Gratchev, I.; Berends, J.; Balasubramaniam, A. Calibration of restitution coefficients using rockfall simulations based on 3D photo-grammetry model: A case study. *Nat. Hazards* **2015**, *78*, 1931–1946. [CrossRef]
16. Fityus, S.; Giacomini, A.; Thoeni, K. The Influence of Shape on the Inherent Rolling Potential of Loose Rocks. In *Engineering Geology for Society and Territory—Volume 2: Landslide Processes*; Springer International Publishing: Cham, Switzerland, 2015; pp. 2045–2048.
17. Huang, R.; Liu, W.; Zhou, J.; Pei, X. Experimental field study of movement characteristics of rock blocks falling down a slope. *J. Earth Sci.* **2010**, *21*, 330–339. [CrossRef]
18. Choi, Y.; Lee, J.Y.; Lee, J.; Park, H.D. Engineering geological investigation into rockfall problem: A case study of the Seated Seokgayeorae Image carved on a rock face at the UNESCO World Heritage site in Korea. *Geosci. J.* **2009**, *13*, 69–78. [CrossRef]
19. Cui, S.-H.; Pei, X.-J.; Huang, R.-Q. Rolling motion behavior of rockfall on gentle slope: An experimental approach. *J. Mt. Sci.* **2017**, *14*, 1550–1562. [CrossRef]
20. Haas, F.; Heckmann, T.; Wichmann, V.; Becht, M. Runout analysis of a large rockfall in the Dolomites/Italian Alps using LIDAR derived particle sizes and shapes. *Earth Surf. Process. Landf.* **2012**, *37*, 1444–1455. [CrossRef]
21. Corominas, J. The angle of reach as a mobility index for small and large landslides. *Can. Geotech. J.* **1996**, *33*, 260–271. [CrossRef]
22. Evans, S.G.; Hungr, O. The assessment of rockfall hazard at the base of talus slopes. *Can. Geotech. J.* **1993**, *30*, 620–636. [CrossRef]
23. Zhan, W.; Fan, X.; Huang, R.; Pei, X.; Xu, Q.; Li, W. Empirical prediction for travel distance of channelized rock avalanches in the Wenchuan earthquake area. *Nat. Hazards Earth Syst. Sci.* **2017**, *17*, 833–844. [CrossRef]
24. Copons, R.; Vilaplana, J.M.; Linares, R. Rockfall travel distance analysis by using empirical models (Solà d'Andorra la Vella, Central Pyrenees). *Nat. Hazards Earth Syst. Sci.* **2009**, *9*, 2107–2118. [CrossRef]
25. Yang, L.; Zhang, M.; Jiao, W.; Wu, Y.; Zhang, C.; Wang, Z. Influence of intergranular friction weakening on rock avalanche dynamics. *Comput. Geotech.* **2023**, *159*, 105440. [CrossRef]
26. Basson, F.R.P. Rigid body dynamics for rock fall trajectory simulation. In Proceedings of the ARMA US Rock Mechanics/Geomechanics Symposium (ARMA), Chicago, IL, USA, 24–27 June 2012.
27. Glover, J.; Bartelt, P.; Christen, M.; Gerber, W. Rockfall-simulation with irregular rock blocks. In *Engineering Geology for Society and Territory—Volume 2: Landslide Processes*; Springer International Publishing: Cham, Switzerland, 2015; pp. 1729–1733.
28. Gratchev, I.; Saeidi, S. The effect of surface irregularities on a falling rock motion. *Geomech. Geoeng.* **2019**, *14*, 52–58. [CrossRef]
29. Wang, Y.; Jiang, W.; Cheng, S.; Song, P.; Mao, C. Effects of the impact angle on the coefficient of restitution in rockfall analysis based on a medium-scale laboratory test. *Nat. Hazards Earth Syst. Sci.* **2018**, *18*, 3045–3061. [CrossRef]
30. Nagendran, S.K.; Ismail, M.A.M. Analysis of rockfall hazards based on the effect of rock size and shape. *Int. J. Civ. Eng.* **2019**, *17*, 1919–1929. [CrossRef]
31. Verma, A.K.; Sardana, S.; Singh, T.N.; Kumar, N. Rockfall analysis and optimized design of rockfall barrier along a strategic road near Solang Valley, Himachal Pradesh, India. *Indian Geotech. J.* **2018**, *48*, 686–699. [CrossRef]

32. Ji, Z.-M.; Chen, T.-L.; Wu, F.-Q.; Li, Z.-H.; Niu, Q.-H.; Wang, K.-Y. Assessment and prevention on the potential rockfall hazard of high-steep rock slope: A case study of Zhongyuntai mountain in Lianyungang, China. *Nat. Hazards* **2023**, *115*, 2117–2139. [CrossRef]
33. Tuan, N.Q. Analysis of rock slope failure and rockfall for preliminary hazard assessment of the cliff at Chau Thoi Quarry. In Proceedings of the International Conference on Innovations for Sustainable and Responsible Mining—ISRM 2020, Hanoi, Vietnam, 15–17 October 2020; Volume 2, pp. 230–249.
34. He, Y.; Nie, L.; Lv, Y.; Wang, H.; Jiang, S.; Zhao, X. The study of rockfall trajectory and kinetic energy distribution based on numerical simulations. *Nat. Hazards* **2021**, *106*, 213–233. [CrossRef]
35. Zhang, Y.; Shao, J.; Liu, Z.; Shi, C. Numerical study on the dynamic behavior of rock avalanche: Influence of cluster shape, size and gradation. *Acta Geotech.* **2023**, *18*, 299–318. [CrossRef]
36. Wang, S.; Yuan, Y.; Zhou, A.; Yin, C. Environmental Study on Analysis of Characteristic Parameters of Rockfall Movement Based on Field Riprap Test and Establishment of SVM and LM-BPNN Prediction Models. *Ekoloji* **2019**, *28*, 3319–3326.
37. Caviezel, A.; Ringenbach, A.; Demmel, S.E.; Dinneen, C.E.; Krebs, N.; Bühler, Y.; Christen, M.; Meyrat, G.; Stoffel, A.; Hafner, E.; et al. The relevance of rock shape over mass—Implications for rockfall hazard assessments. *Nat. Commun.* **2021**, *12*, 5546. [CrossRef] [PubMed]
38. Torsello, G.; Vallero, G.; Castelli, M. The role of block shape and slenderness in the preliminary estimation of rockfall propa-gation. In *IOP Conference Series: Earth and Environmental Science: Proceedings of the Mechanics and Rock Engineering, from Theory to Practice, Turin, Italy, 20–25 September 2021*; IOP Publishing: Bristol, UK, 2021; Volume 833, p. 012177.
39. Liu, Y.; Hu, L.; Bai, G.F. Study on the behavior of a single particle rolling down on sidestep. *J. Shandong Univ. (Sci. Ed.)* **2017**, *52*, 70–74+84.
40. Chau, K.T.; Chan, L.C.P.; Wu, J.J.; Liu, J.; Wong, R.H.C.; Lee, C.F. Experimental studies on rock-fall and debris flow. In *One Day Seminar on Planning, Design and Implementation of Debris Flow and Rockfall Hazards Mitigation Measures*; Wiley: Hong Kong, China, 1998; pp. 115–128.
41. Pei, X.; Huang, R.; Pei, Z.; Dong, X. Analysis on the movement characteristics of Rolling Rock on slopes caused by intensitive earthquake. *J. Eng. Geol.* **2011**, *19*, 498–504.
42. Siming, H.; Weilin, Z.; Xiong, Z.; Suiwang, J.; Qiang, C. Research on rollfall impact of Chediguan bridge pier, Duwen road. *Chin. J. Rock Mech. Eng.* **2013**, *32* (Suppl. S2), 3421–3427.
43. Gong, S.Q. Research on the Influence of Shape, Mass and Feature of Slope to Movement Characteristic of Rockfall. Master's Thesis, Chongqing Jiaotong University, Chongqing, China, 2014.
44. Wong, L.N.Y.; Tang, Z. Preliminary estimation of rock-fall lateral dispersion by laboratory test. *J. Rock Mech. Geotech. Eng.* **2023**. [CrossRef]
45. Fityus, S.; Giacomini, A.; Buzzi, O. The significance of geology for the morphology of potentially unstable rocks. *Eng. Geol.* **2013**, *162*, 43–52. [CrossRef]
46. Cui, T.; Liu, J.; Yang, L.; Zhang, D.; Zhang, R.; Lan, W. Experiment and simulation of rolling friction characteristic of corn seed based on high-speed photography. *Trans. Chin. Soc. Agric. Eng.* **2023**, *29*, 34–41. (In Chinese)
47. Ge, Y.; He, X.R.; Yuan, X.Q.; Pu, X.Y.; Meng, L.D.; Wang, H.K.; Huang, Y.Y. Analysis of rockfall hazards stopping position and energy dissipation based on orthogonal experiment. In Proceedings of the 7th International Conference on Energy Materials and Environment Engineering (ICEMEE 2021), Zhangjiajie, China, 23–25 April 2021; Voume 261, p. 01004.
48. Azzoni, A.; de Freitas, M.H. Experimentally gained parameters, decisive for rock fall analysis. *Rock Mech. Rock Eng.* **1995**, *28*, 111–124. [CrossRef]
49. Su, Y.F.; Bhattacharya, S.; Lee, S.J.; Lee, C.H.; Shin, M. A new interpretation of three-dimensional particle geometry: MAVL. *Transp. Geotech.* **2020**, *23*, 100328. [CrossRef]
50. Hu, J.; Li, S.; Shi, S.; Li, L.; Zhang, Q.; Liu, H.; He, P. Experimental study on parameters affecting the runout range of rockfall. *Adv. Civ. Eng.* **2018**, *2018*, 4739092. [CrossRef]